Published in final edited form as:
Phys Med Biol. 2013 February 7; 58(3): 429–449. doi:10.1088/0031-9155/58/3/429.

Single-scan dual-tracer FLT+FDG PET tumor characterization

Dan J Kadrmas[1,2], **Thomas C Rust**[1], and **John M Hoffman**[1,2]

[1]Utah Center for Advanced Imaging Research, University of Utah, Salt Lake City, UT, USA

[2]Huntsman Cancer Institute, University of Utah, Salt Lake City, UT, USA

Abstract

Rapid multi-tracer PET aims to image two or more tracers in a single scan, simultaneously characterizing multiple aspects of physiology and function without the need for repeat imaging visits. Using dynamic imaging with staggered injections, constraints on the kinetic behavior of each tracer are applied to recover individual-tracer measures from the multi-tracer PET signal. The ability to rapidly and reliably image both ^{18}F-fluorodeoxyglucose (FDG) and ^{18}F-fluorothymidine (FLT) would provide complementary measures of tumor metabolism and proliferative activity, with important applications in guiding oncologic treatment decisions and assessing response. However, this tracer combination presents one of the most challenging dual-tracer signal-separation problems—both tracers have the same radioactive half-life, and the injection delay is short relative to the half-life and tracer kinetics. This work investigates techniques for single-scan dual-tracer FLT+FDG PET tumor imaging, characterizing the performance of recovering static and dynamic imaging measures for each tracer from dual-tracer datasets. Simulation studies were performed to characterize dual-tracer signal-separation performance for imaging protocols with both injection orders and injection delays of 10–60 min. Better performance was observed when FLT was administered first, and longer delays before administration of FDG provided more robust signal-separation and recovery of the single-tracer imaging measures. An injection delay of 30 min led to good recovery ($R > 0.96$) of static image values (e.g. SUV), K_{net}, and K_1 as compared to values from separate, single-tracer time-activity curves. Recovery of higher order rate parameters (k_2, k_3) was less robust, indicating that information regarding these parameters was harder to recover in the presence of statistical noise and dual-tracer effects. Performance of the dual-tracer FLT(0 min)+FDG(32 min) technique was further evaluated using PET/CT imaging studies in five patients with primary brain tumors where the data from separate scans of each tracer were combined to synthesize dual-tracer scans with known single-tracer components; results demonstrated similar dual-tracer signal recovery performance. We conclude that rapid dual-tracer FLT+FDG tumor imaging is feasible and can provide quantitative tumor imaging measures comparable to those from conventional separate-scan imaging.

Introduction

Rapid multi-tracer PET techniques aim to image two or more tracers in a single scan, characterizing multiple aspects of function without requiring repeat scanning sessions separated by hours or days. Since all PET tracers give rise to indistinguishable 511 KeV annihilation photon pairs, there is no *explicit* information in the PET coincidence-pair measurement identifying which coincidence event arose from which tracer. As such, single-scan multi-tracer PET imaging cannot provide measurements identical to conventional separate, single-tracer scans. However, using dynamic imaging with tracer administrations

kadrmas@ucair.med.utah.edu.

staggered in time, constraints on the kinetic behavior of each tracer can be applied to predict each tracers' contribution to the multi-tracer PET signal (Huang *et al* 1982, Koeppe *et al* 1998, 2001, 2004, Hoegerle *et al* 1998, Ikoma *et al* 2001, 2004, Converse *et al* 2004, Wilson *et al* 2004, Kadrmas and Rust 2005, Verhaeghe *et al* 2005, Rust and Kadrmas 2006, El Fakhri *et al* 2006, Rust 2007, Black *et al* 2008, 2009, Gao *et al* 2009, Joshi *et al* 2009, Figueiras *et al* 2009, Kadrmas *et al* 2010). Signal-separation algorithms, where kinetic constraints are used to model or predict the contribution from each tracer as a function of time, can then be applied to recover estimates of each individual tracer (Kadrmas *et al* 2010). While some information is irretrievably lost by temporally overlapping multi-tracer PET imaging, certain information about each component tracer can be reliably recovered (Kadrmas and Rust 2005). Moreover, the recoverable information often includes the targeted imaging measure(s) of interest, i.e. the standardized uptake value (SUV), wash-in rate parameter (K_1) and certain kinetic macroparameters such as the net uptake. The effectiveness of the single-scan multitracer PET approach depends critically upon the tracers used, their radioactive half-lives, their kinetic behaviors in the target imaging volumes, the injection timing and dynamic scanning protocol, and the dual-tracer signal-separation algorithm used. As such, the multitracer technique needs to be separately optimized and evaluated for each tracer combination and imaging application under consideration. In related work, approaches are also being studied for tracer pairs where one tracer is labeled with a radioisotope that emits a prompt high energy gamma in conjunction with the positron, facilitating differentiation of the tracers via triple-coincidence detection of the prompt gamma along with the positron annihilation photons (Andreyev and Celler 2011, Miyaoka *et al* 2011, Gonzalez *et al* 2011, Sitek *et al* 2011), and there is evidence that this additional information may aid in the signal-separation process when using tracer combinations that include such radioisotopes.

Rapid multi-tracer PET has great potential for personalized oncology, where characterization of multiple aspects of tumor physiology and function would provide a wealth of information for improved prognostication, guiding selection of targeted therapies and assessing tumor response. The ability to rapidly and reliably image both ^{18}F-fluorodeoxyglucose (FDG) and ^{18}F-fluorothymidine (FLT) would perhaps have the greatest immediate impact, as characterization of tumor metabolism and proliferative activity provides complementary and relevant information for oncologic treatment decisions and has received much recent interest (Kobe *et al* 2012, Herrmann *et al* 2012, Enslow *et al* 2012, Zander *et al*2011, Xu *et al* 2011, Vera *et al* 2011, Ott *et al* 2011, Kahraman *et al* 2011, Hoshikawa *et al* 2011, Yang *et al* 2010, Yamamoto *et al* 2008, Tian *et al* 2008). Imaging of two ^{18}F-labeled tracers ($T_{1/2}$ = 109.77 m) also avoids the logistical challenges of tracer access and delivery for shorter-lived tracers. However, since both tracers are labeled with relatively long-lived ^{18}F and experience prolonged tumor uptake, this pair of tracers presents one of the most challenging signal-separation problems for single-scan multi-tracer PET where neither differences in radioactive half-life nor rapid clearance facilitate recovery of individual-tracer components.

Previous work on rapid multi-tracer PET has included studies on tracers with different half-lives (Huang *et al* 1982, Ikoma *et al* 2004, Kadrmas and Rust 2005, Black and Kadrmas 2007, Black *et al* 2009, Figueiras *et al* 2009), and also dual-tracer pairs with the same half-life where the duration of the delay between tracer injections was of the order of the radioactive half-life (Koeppe *et al* 1998, 2001, Kadrmas and Rust 2005, Rust and Kadrmas 2006, Black *et al* 2008, Joshi *et al* 2009)—e.g. shorter-lived isotopes such as ^{11}C ($T_{1/2}$ = 20.38 m) and ^{62}Cu ($T_{1/2}$ = 9.67 m). Related investigations on dual-injection rest+stress myocardial perfusion PET have reported good performance with both ^{13}N-($T_{1/2}$ = 9.97 m) and ^{18}F-labeled tracers (Rust *et al* 2006, Kadrmas *et al* 2012), where the high first-pass extraction and rapid blood clearance of these flow tracers mitigate the challenges of dual-

tracer signal-separation. However, the study of dual-tracer PET where the half-lives and tracer kinetics are long relative to the injection delay (as with FLT+FDG imaging) has not yet been reported.

This work characterizes the feasibility and performance of rapid dual-tracer FLT+FDG tumor imaging, studying a number of dual-tracer dynamic imaging sequences and evaluating performance for recovering static and dynamic imaging measures within regions-of-interest (ROIs) for each tracer from dual-tracer datasets. Simulation experiments were performed to characterize the effects of varying the tracer injection order and timing on dual-tracer time-activity curve fits and parameter estimation, establishing the technical feasibility and main limitations of the single-scan dual-tracer FLT+FDG PET imaging approach. Detailed evaluations were then performed for characterizing tumor SUV, kinetic macroparameters and microparameters for dual-tracer FLT and FDG imaging in five patients with primary brain tumors studied under an investigator-initiated clinical trial. In each case, dual-tracer performance was evaluated in terms of its ability to recover parameter estimates that match those computed from separate single-tracer imaging with each tracer.

Methods

The principle of multi-tracer PET signal separation is to model constraints on the kinetic behavior of each tracer in order to estimate each tracers' contribution to the multi-tracer PET signal. When using dynamic imaging with tracer administrations staggered in time, such modeling can be used to predict the timecourse of activity for each constituent tracer at each timepoint. Signal-separation can be performed either explicitly or implicitly: the dynamic imaging signal can be explicitly separated into individual-tracer signals analogous to separate single-tracer imaging, or alternatively the multi-tracer signal can be processed directly to estimate imaging measures (e.g. kinetic parameters) for each tracer in a single step. In both cases, performance is dependent upon the tracer kinetics, tracer injection order and injection delay. We first characterize and optimize the dual-tracer FLT+FDG dynamic imaging sequence using a series of dual-tracer time-activity curve simulation studies. The most promising approach is then evaluated in more detail using clinical imaging data in patients with primary brain tumors, which introduces noise and imaging effects as well as actual *in vivo* tracer kinetics which may be completely consistent with the kinetic models used for the signal-separation process.

Simulation experiments

The simulation studies were based on a single 120 min long dual-tracer scan with staggered injections of FDG and FLT. In our experience, cancer patients vary widely in their ability to tolerate long scans, and 120 min represents the high end of this range. As such, it was deemed appropriate for determining the feasibility of the approach and characterizing the effects of changing tracer injection order and timing. The patient study evaluations used a shorter scan duration of 104 min, which in our experience is generally tolerable by the majority of patients enrolled in our clinical imaging trials. Twelve simulation experiments were performed, corresponding to both injection orders (FDG first and FLT first) with injection delays of 10–60 min for the second tracer in 10 min increments. For each case, a population of 200 different time-activity curves (TACs) were simulated for each tracer for the two-tissue compartment 3-rate parameter '3 K' compartment models ($k_4 = 0$) shown in figure 1. Briefly, K_1 for each tracer represents a combination of delivery to the tissue (blood flow) coupled with diffusion across intercellular space plus transport across the cell membrane (via glucose transporters for FDG, and via pyrimidine transporters for FLT). The washout parameter k_2 represents essentially the reverse of these processes, and k_3 represents phosphorylation (via hexokinase for FDG, and via thymidine kinase for FLT). The 3 K model was used here for several reasons—dual-tracer 3 K + 3 K modeling with ^{18}F-labeled

tracers has not previously been reported, and the 3 K model is appropriate for both FDG and FLT in many cases. The patient evaluations included an additional evaluation of using the 3 K model for FDG and 4 K ($k_4 \neq 0$) model for FLT; in which case the FLT k_4 parameter represents dephosphorylation of FLT-5′-P. Notably, radioactive decay (λ) was included in the models rather than being pre-corrected in the data, as decay correction cannot be performed in multi-tracer PET prior to signal-separation because the proportion of each tracer (and hence its decay-correction factor) is not known prior to the signal-separation.

The plasma input functions (metabolite-corrected for FLT (Shields *et al* 2005)) for each tracer were selected based on representative patient studies for a 10 mCi administration of FDG and 5 mCi administration of FLT; as such, the data modeled a lower dosage of FLT consistent with our clinical research practices due to safety concerns for FLT regarding the potential for liver toxicity at higher doses (Spence *et al* 2008, Turcotte *et al* 2007). This difference in tracer activity levels has implications for the degree of tracer-overlap and dual-tracer performance for the various imaging protocols. The kinetic parameters used for the populations of 200 TACs for each tracer were randomly drawn from representative populations based on research imaging studies performed at our institution with both tracers in patients with various solid malignancies. Certain parameter values were correlated in these populations. For example, the mean value of k_2 was set equal to the randomly sampled value of K_1 divided by 0.9 (corresponding to an initial volume-of-distribution $K_1/k_2 \approx 0.9$), and the randomly sampled value of k_2 varied about this K_1-dependent mean value.

Gaussian-like noise was added to the simulated TACs for each tracer. Here, the noise levels were selected to match those observed in the patient datasets as closely as possible, and the relative noise variance for each timeframe accounted for both the timeframe duration and radioactive decay. For each timeframe a Gaussian noise sample was first generated. If the resulting noise sample was non-negative, the result was kept; however, if the result was negative it was discarded and another noise sample was generated. This resulted in non-negative Gaussian-like noise that was representative of (but not exactly identical to) the noise present in TACs recovered from PET images reconstructed with the iterative ordered-subsets expectation-maximization algorithm. The TACs were then shifted in time as needed for each injection order and delay, and then added to form dual-tracer TACs. The corresponding individual-tracer TACs for each case were also stored and processed to represent conventional separate-scan TACs to be used as the gold standard for evaluating dual-tracer signal-separation performance.

The dynamic imaging sequence varied with the injection delay, with rapid sampling both at time zero (administration of first tracer) and the time $T_{inj}^{(2)}$ (administration of the second tracer). Here, the base sampling schedule consisted of 39 timeframes over 2 h: 6 × 10 s, 4 × 15 s, 4 × 30 s, 6 × 60 s, 5 × 120 s, 8 × 300 s, 6 × 600 s. This sampling schedule was restarted at the time of administration of the second tracer for the given injection delay. The single-tracer TACs were simulated directly onto this sampling schedule for each test case so that they could be directly added to form dual-tracer TACs, and also so that there were no differences in the sampling schedules that could complicate comparison of recovered and single-tracer TACs during the analysis. As such, the dual-tracer TACs and corresponding single-tracer TACs were exactly paired in terms of both signal and noise. The dual-tracer TACs were processed according to the signal-separation algorithms described in the next section, and the single-tracer TACs were processed in the analogous single-tracer manner to obtain SUVs and kinetic parameter estimates for each case.

Dual-tracer processing for signal-separation

The kinetic constraints used for multi-tracer signal-separation can be applied via a number of methods (Kadrmas and Rust 2005, Kadrmas *et al* 2010). Perhaps the most robust approach is parallel multi-tracer compartment modeling (Koeppe *et al* 2001, Ikoma *et al* 2004, Kadrmas and Rust 2005, Kadrmas *et al* 2010), where each tracer's estimated kinetic behavior is constrained to match a compartment model driven by an appropriate input function. Note that no assumptions as to the values of the kinetic parameters of the models need be made—the act of fitting the multi-tracer compartment models to the data imposes the necessary constraints. When the desired imaging endpoints are kinetic parameters themselves, the signal-separation can be performed in a single step through combined application and estimation of kinetic parameters for each tracer; we refer to this as 'implicit' signal-separation, as the dual-tracer TACs are not explicitly separated into individual-tracer components. On the other hand, when the desired imaging endpoints are static measures (e.g. images of each tracer or standardized uptake values (SUVs)), then a two-step 'explicit' signal-separation process is applied where the dual-tracer TAC is first separated into estimated single-tracer components. The recovered components are then processed to obtain the static imaging measure, for example, by integrating late timeframes of the separates datasets to form a static image.

The dual-tracer compartment model can be written as

$$R^{\text{Dual}}(t) = \sum_{n=\text{FLT,FDG}} C^{(n)}\left(t, b^{(n)}(t), \left\{k_i^{(n)}\right\}, \lambda^{(n)}\right), \quad (1)$$

where $R^{\text{Dual}}(t)$ is the dual-tracer time-activity curve, $b^{(n)}(t)$ is the input function for tracer n, $\left\{k_i^{(n)}\right\}$ is the set of kinetic rate parameters for tracer n, $\lambda^{(n)}$ is the radioactive decay constant for tracer n and $C^{(n)}\left(t, b^{(n)}(t), \left\{k_i^{(n)}\right\}\right)$ is the modeled activity concentration for tracer n in the sum of extravascular tissue compartments. For simplicity and to retain focus on dual-tracer effects, we have chosen not to include terms for input function delay, dispersion, partial-volume effects or whole-blood components; although such terms could easily be included in the model as desired. The model can be discretized, taking into account that the PET scanner measures the average activity concentration over the timeframe duration, as

$$R_j^{\text{Dual}} \equiv \frac{1}{\left(t_{j2} - t_{j1}\right)} \int_{t_{j1}}^{t_{j2}} R^{\text{Dual}}\left(\tau; \left\{b^{(n)}(t)\right\}, \left\{k_i^{(n)}\right\}, \left\{\lambda^{(n)}\right\}\right) d\tau, \quad (2)$$

where j is the timeframe index, and t_{j1}, t_{j2} represent the timeframe start and end times, respectively.

Fitting the dual-tracer compartment model consists of simultaneously estimating all rate parameters $\left\{k_i^{(n)}\right\}$ for both tracers n = FLT, FDG according to the criterion of minimizing an objective function such as the weighted sum-squared error:

$$\text{WSSE} = \sum_{j=1}^{T} w_j \left(\widehat{R}_j - \tilde{R}_j\right)^2, \quad (3)$$

where w_j are the weights for each timeframe, and $\tilde{R}_j$ and $\widehat{R}_j$ represent the measured (noisy) and fitted activity concentrations, respectively. Here three rate parameters (K_1 - k_3) were used for each tracer for the simulations, and the patient data were analyzed using three parameters for FDG and both three ($k_4 = 0$) and four ($k_4 = 0$) rate parameters for FLT.

For single-tracer fitting, the weights were selected to take into account the timeframe duration, the effects of signal-loss due to radioactive decay, and incorporated an arbitrary scale factor a that facilitated dual-tracer signal-separation:

$$w_j = a\left(t_{j2} - t_{j1}\right) e^{+\lambda\left(t_{j1}+t_{j2}\right)/2.0}. \quad (4)$$

These weights (excluding the a scale factor) were inversely proportional to the variance of the Gaussian-like noise added to the simulations (up to the non-negativity constraint placed on the simulated noise as described above). For dual-tracer modeling, only a single tracer is present from time 0 until the time that the second tracer is administered $\left(T_{inj}^{(2)}\right)$, beyond which the dual-tracer TAC contains components from both tracers. We've found that it can be helpful to weight the single-tracer portion of the curve more heavily than the dual-tracer portion of the curve, which effectively focuses the fit of tracer 1's kinetic parameters more heavily on the unaffected single-tracer portion of the curve. This is done by making the scale factor a time-dependent:

$$\alpha_j = \begin{cases} \alpha_1 | t_j < T_{inj}^{(2)} \\ \alpha_2 | t_j \geq T_{inj}^{(2)} \end{cases} . \quad (5)$$

Setting a_1 large relative to a_2 increasing the emphasis of tracer 1's fitted parameters on the single-tracer portion of the curve, up to the limit where $a_1 \gg a_2$ effectively sets tracer 1's fit solely on the single-tracer portion of the curve. In the work presented here, we used $a_1 = 10$ and $a_2 = 1$.

Implicit signal-separation—Dual-tracer compartment model fits were performed on all simulated dual-tracer TACs in order to estimate kinetic rate parameters for both FLT and FDG in a single step. Fitting was performed using the recently developed Reduced Parameter Space Kinetic Modeling technique (Kadrmas and Oktay 2012, Oktay and Kadrmas 2012) with an exhaustive search algorithm, which guarantees identification of the true global minimum fit to within the assigned precision of the search algorithm. Briefly, the Reduced Parameter Space modeling technique reformulates the modeling equations to maximally separate the linear and nonlinear aspects, and the separable nonlinear least-squares technique is then applied to constrain the solution space to only include solutions that optimize the fitting criterion in the linear sense. The resultant formulations bear many similarities with the basis functions from plasma input compartment (BAFPIC) techniques (Hong *et al* 2011, Hong and Fryer 2010), and the fits can be performed using both exhaustive search and iterative gradient-descent fitting algorithms. The parameter space reduction is particularly useful for multi-tracer compartment modeling where the number of unknowns and complexity is significantly larger than for single-tracer modeling. The fitted kinetic parameter estimates were constrained to be within the range non-negative, and a search precision of 0.001 min^{-1} was used. The same fitting approach was used to fit the constituent single-tracer TACs, providing the single-tracer standard for comparing dual-tracer estimates.

Explicit signal-separation—In order to obtain static image values, e.g. tumor SUVs, the dual-tracer TACs were explicitly separated to recover estimated TACs for the FLT and FDG components, which were then integrated from 50 to 60 min post-injection of each tracer in order to obtain static values and scaled for conversion to SUV (*ad hoc* scale factors used for the simulated data). Here, the dual-tracer fits were used to predict each tracer's contribution

to the dual-tracer TAC, and the original noisy TAC was then separated according to the predicted proportion from each tracer:

$$\breve{R}_j^{(n)} = \left(\frac{\widehat{R}_j^{(n)}}{\widehat{R}_j^{\mathrm{FLT}} + \widehat{R}_j^{\mathrm{FDG}}} \right) \tilde{R}_j^{\mathrm{Dual}}, \quad (6)$$

where $\breve{R}_j^{(n)}$ is the recovered TAC for tracer n, and $\widehat{R}_j^{(n)}$ is the predicted TAC for tracer n obtained by simulating single-tracer TACs for each tracer using the best-fit parameters from the dual-tracer fit. This approach separates the measured dual-tracer data, including the noise present, into estimated components for each tracer. A different alternative would be to simply use the simulated TACs $\widehat{R}_j^{(n)}$ as the recovered estimates for each tracer. The primary difference is that the former case utilizes the kinetic model to guide the signal-separation whilst permitting any inconsistencies and noise present in the data to remain in the recovered estimates, whereas the latter case restricts the recovered tracer signals to be exactly consistent with the kinetic models used. As such, we believe the approach described in equation (6) to be more conservative and less critically dependent on the accuracy of the kinetic models.

Evaluation in patients with primary brain tumors

The dual-tracer FLT+FDG imaging technique was further evaluated in five patients with primary brain tumors who received dynamic FLT and FDG PET/CT scanning under a prospective research trial approved by the University of Utah Institutional Review Board. Subjects were identified as having primary brain tumors greater than 1 cm^3 by conventional imaging (contrast-enhanced T1 MRI) and were screened to ensure that they could safely and willingly undergo repeat dynamic imaging for up to 2 h with each tracer on separate days. For each scan, the subject was positioned on the imaging table with head immobilized in a custom-built head holder designed for reproducible positioning (Chapman *et al* 2008); while this head holder did not guarantee perfect repositioning, it did serve to reposition the head in a similar orientation with matched vertical, lateral and axial positioning. Dynamic single-tracer PET/CT scans with FLT (4.9 ± 0.1 mCi) and FDG (7.8 ± 0.01 mCi) were acquired on back-to-back days on a Discovery ST PET/CT scanner (GE Healthcare) operated in fully 3D mode with listmode acquisition. Blood samples were acquired to characterize the input function for each tracer using the arterialized heated-hand venous sampling technique of Copeland *et al* (1992) and Sonnenberg and Keller (1982), acquiring 20–24 samples at slowing intervals following tracer injection. Samples were separated into plasma and whole-blood components, and FLT metabolites were identified using the method described in Shields *et al* (2005). For the dual-tracer processing, it was assumed that the input function for each tracer could be recovered from dual-tracer samples using, e.g., chemical separation of the blood samples for each tracer, population-based methods or other extrapolation techniques. Separation of dual-tracer input functions from arterial blood samples has previously been studied for other tracers (Kudomi *et al* 2007). In the case of FLT+FDG imaging, the same techniques used for identification of circulating metabolites from FLT (Shields *et al* 2005) could potentially be used to separate the FLT and FDG inputs; however, further work is necessary to develop and validate such techniques before they can be used in practice.

Though listmode data were acquired, the deadtime correction on this scanner model (Discovery ST PET/CT scanner; GE Healthcare) was dependent on the dynamic imaging sequence specified for the acquisition. In order to permit flexible post-processing with differing dynamic sequences, a specially designed dynamic sequence was specified: A(0–8

min), A(8–16 min), A(16–24 min), A(24–32 min), AB(32–48 min), AB(48–64 min), AB(64–80 min), AB(80–96 min), ABC(96–128 min), where $A = 6 \times 10$ s, 4×15 s, 4×60 s; $B = 4 \times 120$ s; and $C = 4 \times 240$ s. This sequence provided rapid sampling a 0, 8, 16, 24, 32, 48 and 64 min, permitting study of dual-tracer injection delays for each of these times. In addition, the timeframes of each sub-sequence are aligned with the longer duration timeframes so that they could be collapsed to longer timeframes as needed for differing injection delays. This allowed the patient studies to be performed in conjunction with the simulation studies without restricting the patient studies to be applicable to only a single injection timing. After analysis of the simulation studies, the dual-tracer protocol with FLT administered at time 0 min and FDG at time 32 min was selected for the patient study evaluations, and the patient study data were collapsed to that dual-tracer scanning sequence accordingly.

Dynamic scanning with both tracers was successfully performed in all five subjects; however, not all subjects were able to tolerate the full targeted 2 h scan durations. The shortest duration tolerated was 104 min; hence, only the first 104 min of each scan were used in order to maintain consistency. The PET listmode files were then binned to the FLT(0 min)+FDG(32 min) dual-tracer sequence: ABCABCD, where sequences ABC are as defined above and $D = 5 \times 480$ s. This provided fast sampling at 0 min and 32 min and a total duration of 104 min. The FLT data were binned directly onto this sequence, and the FDG data were shifted by 32 min (with leading zeros) and then binned onto the latter portion of the dual-tracer sequence (ABCD).

All images were reconstructed with 2 iterations 21 subsets ordered-subsets expectation-maximization (OSEM) onto 128 × 128 images using 2.34 mm pixels, and no post-reconstruction smoothing filter was applied. The single-tracer datasets were processed separately and used as controls for evaluating dual-tracer performance. Registration of the images from each tracer was assessed visually in transaxial, coronal and sagittal planes and no discrepancies larger than approximately 1 voxel in size were noted based on this visual assessment. The single-tracer images were then added to create corresponding dual-tracer datasets, summing the data from 32 min onward. This approach provided representative dual-tracer datasets with known and paired single-tracer components to be used as standards for comparison, permitting performance evaluations assessing the dual-tracer signal-separation procedure in terms of its ability to recover these single-tracer components. It also provided an experimental design that was insensitive to registration errors between the images for each tracer, as the actual component images for each tracer provided the standards for evaluation of the dual-tracer technique. However, these synthetic dual-tracer data were not perfect representations of actual dual-tracer data because the levels of deadtime and randoms present were somewhat lower than would be encountered in actual dual-tracer scans. The effects of deadtime and random coincidences are well known, however, and corrections for each are well understood and validated. In actual dual-tracer data, slightly higher levels of statistical noise would be present due to somewhat higher deadtimes (e.g. slight loss of counts) coupled with a larger randoms correction.

Twelve ROIs 1.98 ± 1.04 cm^3 (range 0.52–5.80 cm^3) were drawn on the images for each patient, including both tumor and normal brain tissue, and multiple ROIs were used for larger tumors when either the FLT or FDG image (or both) displayed heterogeneity. This provided a total of 60 ROIs for analysis. Time-activity curves for both single- and dual-tracer images were generated for each ROI and processed using the methods described above. The 3 K compartment model ($k_4 = 0$) was used for FDG, and both 3 K and 4 K models ($k_4 \neq 0$) were used for FLT as described in the Results section. Each dual-tracer TAC was fit and processed using explicit signal-separation to recover estimates of the component FLT and FDG TACs, which were then integrated from 62 to 72 min post-

injection and scaled to obtain static SUV values. The best-fit kinetic parameters from the dual-tracer fits were also stored for each tracer and analyzed, with kinetic macroparameters computed from the best-fit microparameters: $K_{net} = K_1 k_3/(k_2 + k_3)$ and initial volume-of-distribution K_1/k_2. Corresponding fits and processing were performed for the separate single-tracer TACs as well. Linear regression analysis was then used to compare and analyze each imaging measure recovered from dual-tracer data versus from single-tracer data.

Results

Injection order and timing

Figure 2 shows example-simulated dual-tracer time-activity curves, compartment model fits and explicit signal-separation to recover individual-tracer TAC estimates. The separation and recovery of the individual-tracer components deserve some comment. Using the explicit signal-separation algorithm, the noise in the original dual-tracer TAC is split between the tracers in proportion to the estimated signal contributions from each tracer. For the second tracer, FDG in this example, the recovered TAC is very similar to what would be obtained from conventional single-tracer imaging. However, the recovered TAC for the first tracer (FLT in this example) contains both fast-sampling and high noise for the timeframes concurrent with the injection of the second tracer. This noise structure has a dramatic appearance on the recovered FLT TAC; however, collapsing these timeframes from rapid sampling (i.e. 10 s and 15 s timeframes) to a typical single-tracer sampling schedule (i.e. 5–10 min at this point after injection of the tracer) would restore the noise appearance to be much more typical of conventional single-tracer imaging.

Linear regression analysis was performed to assess the ability of the single-scan dual-tracer technique to obtain the same imaging endpoints (SUV, K_{net}, K_1) as were obtained from the conventional single-tracer datasets. Figure 3 summarizes the simulation results for recovery of K_{net} for both tracers as a function of the injection order and the injection delay. Recovery of FDG K_{net} was not highly dependent on the injection order or delay; however, recovery of FLT K_{net} was sensitive to both. Overall performance was relatively poor for the shorter injection delays, and improved markedly for delays of 30 min and longer. This is consistent with the postulate that, when using kinetics-based dual-tracer signal-separation, better performance is obtained when the injection delay is long enough that the initial ‘fast’ kinetic phase for the first tracer is largely resolved prior to administration of the second tracer. Recovery of K_{net} for both tracers also rolled off slightly for the longest delays (50–60 min), which is an effect of using a fixed 120 min scan duration—only 60 min of data were acquired after injection of the second tracer for this longest delay, providing a shortened dynamic dataset after tracer administration with slightly degraded kinetic modeling performance.

Recovery of FLT K_{net} was markedly better when FLT was administered first, as compared to the opposite injection order, for delays of 30 min and longer. This is in part due to the fact that the FLT activity and uptake tended to be lower than that for FDG; hence, the FLT-first datasets provided a smaller degree of tracer overlap than the FDG-first datasets. Recall that the simulations modeled a 5 mCi injection of FLT versus a 10 mCi injection of FDG (due to safety considerations for FLT); in addition, FLT tends to have lower tumor uptake than FDG in general. These effects were included in the simulations via the magnitude of the FLT input function and population of kinetic parameters used. It is important to note that effects such as these may differ somewhat for different target imaging volumes, for example, FLT experiences greater bone and liver uptake than FDG. Special consideration should be paid to dual-tracer protocol design when the target tumors fall within such organs.

Given these results, we focus the remainder of the paper upon the dual-tracer FLT+FDG imaging technique with FLT administered first and FDG administered after an ~30 min delay (30 min for the simulation data, and 32 min for the patient data due to the special dynamic imaging sequence used for the patient acquisitions).

FLT(0 min)+FDG(30 min) performance

Figure 4 shows scatter plots for recovering static SUVs for each tracer from the FLT(0 min) +FDG(30 min) dual-tracer protocol. The explicit signal-separation procedure described in the Methods section was used here, and the recovered TACs for each tracer were integrated from 50 to 60 min and scaled to provide SUV estimates. Recovery of SUV for both tracers was excellent, with slopes very close to 1.0 and correlation coefficients >0.99. The FDG SUV results in particular were extremely robust. These data demonstrate that the single-scan FLT(0 min)+FDG(30 min) dual-tracer PET technique can provide static-image tumor measures for both tracers that are nearly identical to those from conventional, separate single-tracer scanning. Scatter plots for the recovery of the net-uptake macroparameter for both tracers are also shown in the figure. Again, the linear regression analysis shows very little bias and excellent correlations, demonstrating that the K_{net} macroparameter can also be robustly recovered from single-scan dual-tracer FLT+FDG imaging.

Results for recovery of each tracer's individual rate parameters K_1–k_3 are shown in figure 5. Here K_1 was recovered quite well in general ($R > 0.96$), as were k_2 ($R = 0.938$) and k_3 ($R = 0.918$) for FDG; however, recovery of k_2 and k_3 for FLT was less robust. These higher order rate parameters had subpopulations with good agreement for dual- and single-tracer values, but there were also a number of outliers where values differed significantly. Studying the outliers more closely, it was noted that most FLT datapoints with poor agreement between dual-tracer and single-tracer results corresponded to cases with FLT $K_1 < 0.10$ min^{-1}—i.e. cases with low FLT uptake where the magnitude of the FLT time-activity curve was relatively low. Repeating the linear regression analysis on those data with single-tracer FLT $K_1 \geq 0.10$ min^{-1} gave greatly improved dual versus single-tracer correlations for FLT K_1 ($R = 0.981$), k_2 ($R = 0.964$) and k_3 ($R = 0.912$). It is well known that estimation of individual rate parameters in single-tracer modeling is more sensitive to statistical noise than is estimation of SUVs or macroparameters such as K_{net}, and the above results would suggest that recovery of these parameters from dual-tracer is not robust when FLT tracer uptake is low.

Evaluation in patients with primary brain tumors

The dual-tracer FLT+FDG imaging technique with 32 min FDG delay was evaluated further in five patients with primary brain tumors. In contrast to the simulations, in which the underlying kinetics of the data (up to the statistical noise added) were exactly consistent with the models used for signal-separation, these data contain real-world imaging effects and *in vivo* tracer kinetics for which the kinetic models used are reasonable matches but not exactly consistent. As such, these evaluations with patient data test, in part, the sensitivity of the dual-tracer signal-separation processing to data-model inconsistencies that arise in actual use, as well as the performance characteristics of the dual-tracer imaging in general.

Example reconstructed images are shown in figure 6, providing visual examples of the size and character of the brain tumors used in this study, along with the assessment of overall image quality. Sixty ROIs were drawn over both tumor and normal brain regions and used for the quantitative evaluation of dual-tracer performance for recovering both static and dynamic imaging measures for each region. Example dynamic images are shown in figure 7, along with a representative dual-tracer TAC and fit results. The data and approach were consistent with those for the simulation studies, and no significant differences due to real-

world imaging effects such as partial-volume effect or model-data inconsistencies were noted in the study.

Static imaging measures—Scatter plots comparing recovery of static tumor SUVs from dual-tracer imaging versus single-tracer standards are shown in figure 8, where the signal-separation technique described by equation (6) was used. Excellent recovery of tumor SUVs was observed, with recovered FDG values nearly identical to those for separate-scan imaging (R = 0.999; slope = 1.007) and FLT values slightly less accurately recovered (R = 0.985; slope = 1.003). Similar results were obtained when the dual-tracer SUV estimates were obtained by integrating the fitting time-activity curves for each tracer (as opposed to explicitly separating the noise dual-tracer TAC using equation (6)), resulting in correlation coefficients of 0.995 and 0.988 for FDG and FLT, respectively. The difference here was due to differences in noise propagation when signal-separation is performed explicitly via equation (6) as compared to implicitly using the dual-tracer model fits directly. These results demonstrate that application of the dual-tracer technique for these data did not adversely affect FDG SUV measures, and that significant information regarding FLT SUV was also accurately measured.

Dual 3 K + 3 K kinetic parameters—Figure 9 depicts results for the recovery of kinetic macroparameters using a 3 K model ($k_4 = 0$) for both FDG and FLT, and results for individual rate parameters are listed in table 1. Again, very good recovery of the net-uptake parameter (K_{net}) for both tracers was observed ($R > 0.99$). The figure also includes the macroparameter K_1/k_2, sometimes referred to as the initial volume-of-distribution. This imaging measure was recovered from dual-tracer data with good correlation (R = 0.910 and R = 0.987 for FLT and FDG, respectively) for both tracers, but with moderate bias for FLT (slope = 1.199). Individual kinetic rate parameters for FDG were robustly recovered, with very good correlations and little bias for all parameters. Similarly, FLT K_1 was also well recovered; however, recovery of FLT k_2 and k_3 exhibited moderate bias and lower correlation coefficients, indicating that information regarding these microparameters was somewhat degraded by the single-scan dual-tracer imaging procedure.

Dual 3 K + 4 K performance—The patient study processing was repeated using the 3 K model for FDG ($k_4 = 0$) and 4 K model ($k_4 \neq 0$) for FLT in order to test dual-tracer performance using this more complex kinetic model. Use of the more complex FLT model had very little effect on the recovery of SUV, K_1, K_{net}, and the initial volume-of-distribution K_1/k_2 for both FLT and FDG, with correlations $R > 0.97$ and little bias for all cases. Moderately good recovery of FDG k_2 and k_3 was obtained (R = 0.94 and R = 0.82, respectively), but recovery of FLT k_3 was less robust (R = 0.89 and R = 0.62 for FLT k_2 and k_3, respectively). The FLT dephosphorylation parameter, k_4, was also not accurately recovered ($R < 0.2$), and additional algorithmic and protocol advancements would be needed in order to improve recovery of this parameter. We also studied recovery of the FLT phosphorylation fraction, $K_3/(k_2+k_3)$, from dual-tracer 3 K + 4 K modeling, and found that this parameter was recovered with good correlation (R =0.967) but moderate bias (slope = 0.827, intercept = -0.002 min^{-1}).

Discussion

This work has investigated the potential for ^{18}F-FLT and ^{18}F-FDG to be imaged together in a single scan using rapid multi-tracer PET techniques. The study was designed to evaluate dual-tracer performance in terms of its ability to recover the same imaging measures (SUV, kinetic parameters) as would have been obtained from conventional single-tracer scanning with each tracer. As such, the single-tracer measures were used as gold standards for evaluating dual-tracer signal-recovery performance. No study of the estimability of these

parameters for single-tracer imaging or their value for clinical tasks was performed. Similarly, no blood volume term was included in the models, and no study of the performance of the dual-tracer approach for estimating the blood volume was performed (which would have been complicated by the fact that single-tracer estimates of the blood volume could well be inconsistent for the synthesized dual-tracer study design used in this work). The work studied both dual-tracer 3 K + 3 K ($k_4 = 0$) modeling and dual-tracer 4 K + 3 K ($k_4 \neq 0$ for FLT) modeling, where notably both tracers had the same radioactive half-life and the injection delay was short relative to the half-life and timing of the tracer kinetics. The work did not include study of a blood volume term (f_B), as the synthesized dual-tracer patient data were not sufficiently well registered to provide consistent f_B terms for both tracers. A parallel dual-tracer compartment modeling technique was employed, which included a novel weighting scheme intended to facilitate dual-tracer signal-separation. *Ad hoc* values of the weighting factor were used ($a_1 = 10$ and $a_2 = 1$) and found to provide effective performance; however, additional study and optimization of these parameters were not performed. Recovery of static and dynamic imaging measures for characterizing tumor and normal tissue ROIs was investigated, but voxelwise recovery of separate dynamic images for each tracer was not included as this represents a more challenging signal-separation environment with higher statistical noise; future development of voxelwise separation techniques should be based upon the ROI signal-separation techniques studied in this paper. In addition, the input functions for each tracer were assumed to be known, for example, from blood sampling coupled with chemical separation of the tracers, and issues related to separating the input functions in practice were not addressed.

Whenever quantitative kinetic modeling is performed, the kinetic model(s) should be carefully selected for the given imaging application. These models may differ for different tracers, for different imaging volume(s) and for the various interpretations to be performed. This is true for both single-tracer and rapid dual-tracer imaging when the targeted imaging endpoints include kinetic rate parameters; however, when other imaging endpoints—such as static images or SUVs—are targeted for dual-tracer imaging, the dependence upon kinetic model selection may be somewhat lessened. The models need to be sufficiently accurate to provide multi-tracer signal-separation, but the models themselves are not interpreted. The work presented in this paper is not intended to provide guidance on the selection of kinetic models for FLT or FDG imaging, and individual expertise should be applied to each imaging situation in practice. Several model configurations were studied in this work in order to characterize the performance of the rapid dual-tracer technique under a variety of situations that may apply to different practical applications.

Simulated TACs using realistic input functions and kinetic parameters for each tracer showed that rapid single-scan imaging of this tracer pair is feasible when FLT is administered first and FDG is administered after a delay of 30 min, and dual-tracer imaging FLT(0 min) + FDG(32 min) imaging was evaluated in more detail using PET imaging studies in patients with primary brain tumors. Using a parallel dual-tracer compartment-modeling technique, the SUV ($R \geq 0.99$), K_{net} ($R \geq 0.98$), and K_1 ($R > 0.96$) for both tracers were accurately recovered, providing estimates similar to those from separate single-tracer data. The higher order rate parameters (k_2, k_3) were also accurately recovered for FDG, but these microparameters were not robustly recovered for FLT. We postulate that this is due in part to the relatively high noise sensitivity of these parameters (even for single-tracer imaging), as well as the ill-conditioned nature of recovering subtle differences in the curvature of the retention and washout phases of the temporally overlapping regions of dual-tracer TACs. Use of the more complex compartment model with $k_4 \neq 0$ had little effect on the recovery of SUVs and kinetic macroparameters, but the FLT k_4 parameter itself was not robustly recovered from dual-tracer datasets.

The patient data used in this work was acquired using separate, single-tracer scans with each tracer using dynamic imaging protocols designed to permit the data to be combined to synthesize representative single-scan dual-tracer datasets. Using this approach, the single-tracer components of the dual-tracer datasets were known exactly and provided the gold standards for evaluating the dual-tracer performance (e.g. in terms of its ability to provide the same imaging endpoints as single-tracer data). While representative of dual-tracer data, some aspects of actual dual-tracer scans were present in the synthesized datasets. In actual dual-tracer scans, both the deadtime and rates of random coincidences would be higher than that present in the synthesized data because activity from both tracers would simultaneously contribute to both effects. However, since the tracer administrations are staggered in time, the peak deadtime and randoms rates accompanying each bolus are separated in time and the peak rates are not piled simultaneously. Corrections for deadtime and randoms are well understood, and the moderate increases associated with the rapid dual-tracer technique do not present significant differences. The primary effect would be a moderate increase in statistical noise associated with the somewhat greater magnitude of these corrections for actual dual-tracer data. The synthesized dual-tracer datasets provide an essential evaluation of the rapid dual-tracer technique, as dual-tracer signal-separation is critically dependent upon kinetic constraints for each tracer. As such, it is important to assess the effects of real-data inconsistencies between the actual *in vivo* kinetics and the kinetic models used; comparison of the simulation and patient data results demonstrates that the proposed technique is not highly sensitive to such model-data inconsistencies.

Conclusions

We conclude that rapid dual-tracer FLT+FDG PET for characterizing tumors is feasible in a single ~100 min duration scan when either static imaging measures (SUVs) or kinetic macroparameters (K_{net}, K_1/k_2) are desired for each tracer, but conventional separate-scan imaging may be necessary when estimates of the higher order individual rate constants for FLT are needed. The acquisition of FLT data in addition to FDG using the proposed dual-tracer technique did not have a substantial adverse effect on the quality of the FDG imaging measures. As such, dual-tracer FLT+FDG imaging may provide complementary information regarding tumor proliferation in addition to high quality FDG imaging measures. Additional work is warranted to further optimize and evaluate the dual-tracer FLT+FDG technique for different body imaging volumes and for various imaging applications.

Acknowledgments

This work was supported by grant R01CA135556 from the National Cancer Institute and by seed funding from the Ben B and Iris M Margolis Foundation. This work was also supported by the Huntsman Cancer Institute through its Molecular Imaging Research Program, and it was facilitated by Cancer Center Support Grant 3P30CA042014 from the National Cancer Institute and by the Huntsman Cancer Foundation. The content is solely the responsibility of the authors and does not necessarily represent the official views of the National Cancer Institute or the National Institutes of Health. The authors would like to thank Rock Hadley and Robb Merrill for constructing the head immobilizer repositioning device used for the patient studies. They would also like to thank Regan Butterfield, Britney Beardmore and Paul Christian for assistance in performing the patient studies, taking blood samples and offloading the raw PET data. Finally, the authors would like to thank the anonymous reviewers for their many helpful comments and suggestions that improved the paper.

References

Andreyev A, Celler A. Dual-isotope PET using positron-gamma emitters. Phys. Med. Biol. 2011; 56:4539–56. [PubMed: 21725143]

Black, NF.; Kadrmas, DJ. Measurement of secondary tracers in FDG tumor imaging by rapid multi-tracer PET; IEEE Nuclear Sci. Symp. and Medical Imaging Conf.; Honolulu, Hawaii. 2007; 2007. p. 2825-32.26 October-3 November

Black NF, Mcjames S, Kadrmas DJ. Rapid multi-tracer pet tumor imaging with F-FDG and secondary shorter-lived tracers. IEEE Trans. Nucl. Sci. 2009; 56:2750–8. [PubMed: 20046800]

Black NF, Mcjames S, Rust TC, Kadrmas DJ. Evaluation of rapid dual-tracer (62)Cu-PTSM + (62)Cu-ATSM PET in dogs with spontaneously occurring tumors. Phys. Med. Biol. 2008; 53:217–32. [PubMed: 18182698]

Chapman BE, Minalga ES, Brown C, Roberts JA, Hadley JR. Reducing morphological variability of the cervical carotid artery in serial magnetic resonance imaging using a head and neck immobilization device. J. Magn. Reson. Imaging. 2008; 28:258–62. [PubMed: 18581389]

Converse AK, Barnhart TE, Dabbs KA, Dejesus OT, Larson JA, Nickles RJ, Schneider ML, Roberts AD. PET Measurement of rCBF in the presence of a neurochemical tracer. J. Neurosci. Methods. 2004; 132:199–208. [PubMed: 14706718]

Copeland KC, Kenney FA, Nair KS. Heated dorsal hand vein sampling for metabolic studies: a reappraisal. Am. J. Physiol. 1992; 263:E1010–4. [PubMed: 1443110]

El Fakhri, G.; Sitek, A.; Guerin, B. Simultaneous dual tracer PET using generalized factor analysis of dynamic sequences; IEEE Nuclear Sci. Symp. and Medical Imaging Conf.; San Diego, California. 2006; 2006. p. 2128-30.29 October-1 November

Enslow MS, Zollinger LV, Morton KA, Kadrmas DJ, Butterfield RI, Christian PE, Boucher K, Heilbrun ME, Jensen RL, Hoffman JM. Comparison of F-18 fluorodeoxyglucose and F-18 fluorothymidine positron emission tomography in differentiating radiation necrosis from recurrent glioma. Clin. Nucl. Med. 2012; 37:854–61. [PubMed: 22889774]

Figueiras, FP.; Jimenez, X.; Pareto, D.; Gomez, V.; Llop, J.; Gispert, JD. An evaluation of simultaneous dual-tracer technique for PET static studies; IEEE Nuclear Sci. Symp. and Medical Imaging Conf.; Orlando, Florida. 2009; 2009. p. 3225-9.24 October-1 November

Gao F, Liu H, Jian Y, Shi P. Dynamic dual-tracer PET reconstruction. Inf. Process. Med. Imaging. 2009; 21:38–49. [PubMed: 19694251]

Gonzalez, E.; Olcott, PD.; Bieniosek, M.; Levin, CS. Methods for increasing the sensitivity of simultaneous multi-isotope positron emission tomography; IEEE Nuclear Sci. Symp. and Medical Imaging Conf.; Valencia. 2011; Oct 23-29. 2011 p. 3597-601.

Herrmann K, et al. Comparison of 3′-deoxy-3′-[(1)(8)F]fluorothymidine positron emission tomography (FLT PET) and FDG PET/CT for the detection and characterization of pancreatic tumours. Eur. J. Nucl. Med. Mol. Imaging. 2012; 39:846–51. [PubMed: 22278320]

Hoegerle S, Juengling F, Otte A, Altehoefer C, Moser EA, Nitzsche EU. Combined FDG and [F-18]fluoride whole-body PET: a feasible two-in-one approach to cancer imaging? Radiology. 1998; 209:253–8. [PubMed: 9769840]

Hong YT, Beech JS, Smith R, Baron JC, Fryer TD. Parametric mapping of [18F] fluoromisonidazole positron emission tomography using basis functions. J. Cereb. Blood Flow Metab. 2011; 31:648–57. [PubMed: 20736963]

Hong YT, Fryer TD. Kinetic modelling using basis functions derived from two-tissue compartmental models with a plasma input function: general principle and application to [18F]fluorodeoxyglucose positron emission tomography. Neuroimage. 2010; 51:164–72. [PubMed: 20156574]

Hoshikawa H, Nishiyama Y, Kishino T, Yamamoto Y, Haba R, Mori N. Comparison of FLT-PET and FDG-PET for visualization of head and neck squamous cell cancers. Mol. Imaging Biol. 2011; 13:172–7. [PubMed: 20464518]

Huang SC, Carson RE, Hoffman EJ, Kuhl DE, Phelps ME. An investigation of a double-tracer technique for positron computerized tomography. J. Nucl. Med. 1982; 23:816–22. [PubMed: 6980975]

Ikoma, Y.; Toyama, H.; Suhara, T. Simultaneous quantification of two brain functions with dual tracer injection in PET dynamic study; International Workshop on Quantitation in Biomedical Imaging with PET and MRI; Osaka, Japan. 2004; Jan 26-27. 2004 p. 74-8.

Ikoma, Y.; Toyama, H.; Uemura, K.; Uchiyama, A. In: Seibert, JA., editor. Evaluation of the reliability in kinetic analysis for dual tracer injection of FDG and flumazenil PET study; IEEE Nuclear Sci. Symp. and Medical Imaging Conf.; San Diego, California. 2001; Nov 4-10. 2001 p. 2054-7.

Joshi AD, Koeppe RA, Fessler JA, Kilbourn MR. Signal separation and parameter estimation in noninvasive dual-tracer PET scans using reference-region approaches. J. Cereb. Blood Flow Metab. 2009; 29:1346–57. [PubMed: 19401708]

Kadrmas DJ, Di Bella EVR, Black NF, Rust TC. Rapid multi-tracer PET imaging systems and methods. Dec 7.2010 USA Patent Application 11/690,178. 2010.

Kadrmas, DJ.; Oktay, MB. Rapid multi-tracer PET using reduced parameter space kinetic modeling; IEEE Nuclear Sci. Symp. and Medical Imaging Conf.; Anaheim, California. 2012; 2012. 29 October-3 Novemberat press

Kadrmas DJ, Rust TC. Feasibility of rapid multitracer PET tumor imaging. IEEE Trans. Nucl. Sci. 2005; 52:1341–7.

Kadrmas DJ, Rust TC, Lazewatsky JL, Slomka PJ, Berman DS, Dicarli MF, Sitek A. Single scan rest-stress cardiac PET imaging with flurpiridaz F18. J. Nucl. Med. 2012; 53:140.

Kahraman D, et al. Quantitative analysis of response to treatment with erlotinib in advanced non-small cell lung cancer using 18F-FDG and 3′-deoxy-3′-18F-fluorothymidine PET. J. Nucl. Med. 2011; 52:1871–7. [PubMed: 22065872]

Kobe C, et al. Predictive value of early and late residual (18)F-fluorodeoxyglucose and (18)F-fluorothymidine uptake using different SUV measurements in patients with non-small-cell lung cancer treated with erlotinib. Eur. J. Nucl. Med. Mol. Imaging. 2012; 39:1117–27. [PubMed: 22526960]

Koeppe, RA.; Ficaro, EP.; Raffel, DM.; Minoshima, S.; Kilbourn, MR.; Carson, RE.; Daube-Witherspoon, ME.; Herscovitch, P. Temporally overlapping dual-tracer PET studies Quantitative Functional Brain Imaging with Positron Emission Tomography. Academic; San Diego, CA: 1998.

Koeppe RA, Joshi A, Frey K, Snyder SE, Kilbourn MR, Fessler J. Dual-tracer PET studies without arterial sampling. NeuroImage. 2004; 22:T115–6.

Koeppe RA, Raffel DM, Snyder SE, Ficaro EP, Kilbourn MR, Kuhl DE. Dual-[11C]tracer single-acquisition positron emission tomography studies. J. Cereb. Blood Flow Metab. 2001; 21:1480–92. [PubMed: 11740210]

Kudomi N, Watabe H, Hayashi T, Iida H. Separation of input function for rapid measurement of quantitative CMRO2 and CBF in a single PET scan with a dual tracer administration method. Phys. Med. Biol. 2007; 52:1893–908. [PubMed: 17374918]

Miyaoka, RS.; Hunter, WCJ.; Andreyev, A.; Pierce, L.; Lewellen, TK.; Celler, A.; Kinahan, PE. Dual-radioisotope PET data acquisition and analysis; IEEE Nuclear Sci. Symp. and Medical Imaging Conf.; Valencia. 2011; Oct 23-29. 2011 p. 3780-3.

Oktay MB, Kadrmas DJ. Reduced parameter space formulations for robust kinetic modeling. J. Nucl. Med. 2012; 53:2292.

Ott K, et al. Molecular imaging of proliferation and glucose utilization: utility for monitoring response and prognosis after neoadjuvant therapy in locally advanced gastric cancer. Ann. Surg. Oncol. 2011; 18:3316–23. [PubMed: 21537865]

Rust, TC.; University of Utah. PhD Dissertation. 2007. Advances in rapid multi-tracer positron emission tomography.

Rust TC, Dibella EV, Mcgann CJ, Christian PE, Hoffman JM, Kadrmas DJ. Rapid dual-injection single-scan 13N-ammonia PET for quantification of rest and stress myocardial blood flows. Phys. Med. Biol. 2006; 51:5347–62. [PubMed: 17019043]

Rust TC, Kadrmas DJ. Rapid dual-tracer PTSM+ATSM PET imaging of tumour blood flow and hypoxia: a simulation study. Phys. Med. Biol. 2006; 51:61–75. [PubMed: 16357431]

Shields AF, Briston DA, Chandupatla S, Douglas KA, Lawhorn-Crews J, Collins JM, Mangner TJ, Heilbrun LK, Muzik O. A simplified analysis of [18F]3′-deoxy-3′-fluorothymidine metabolism and retention. Eur. J. Nucl. Med. Mol. Imaging. 2005; 32:1269–75. [PubMed: 15991018]

Sitek, A.; Andreyev, A.; Celler, A. Reconstruction of dual isotope PET using expectation maximization (EM) algorithm; IEEE Nuclear Sci. Symp. and Medical Imaging Conf; Valencia. 2011; Oct 23-29. 2011 p. 4323-6.

Sonnenberg GE, Keller U. Sampling of arterialized heated-hand venous blood as a noninvasive technique for the study of ketone body kinetics in man. Metabolism. 1982; 31:1–5. [PubMed: 6804743]

Spence AM, Muzi M, Link JM, Hoffman JM, Eary JF, Krohn KA. NCI-sponsored trial for the evaluation of safety and preliminary efficacy of FLT as a marker of proliferation in patients with recurrent gliomas: safety studies. Mol. Imaging Biol. 2008; 10:271–80. [PubMed: 18543042]

Tian J, Yang X, Yu L, Chen P, Xin J, Ma L, Feng H, Tan Y, Zhao Z, Wu W. A multicenter clinical trial on the diagnostic value of dual-tracer PET/CT in pulmonary lesions using 3′-deoxy-3′-18F-fluorothymidine and 18F-FDG. J. Nucl. Med. 2008; 49:186–94. [PubMed: 18199618]

Turcotte E, Wiens LW, Grierson JR, Peterson LM, Wener MH, Vesselle H. Toxicology evaluation of radiotracer doses of 3′-deoxy-3′-[18F]fluorothymidine (18F-FLT) for human PET imaging: Laboratory analysis of serial blood samples and comparison to previously investigated therapeutic FLT doses. BMC Nucl. Med. 2007; 7:3. [PubMed: 17608943]

Vera P, Bohn P, Edet-Sanson A, Salles A, Hapdey S, Gardin I, Menard JF, Modzelewski R, Thiberville L, Dubray B. Simultaneous positron emission tomography (PET) assessment of metabolism with (1)(8)F-fluoro-2-deoxy-d-glucose (FDG), proliferation with (1)(8)F-fluoro-thymidine (FLT), and hypoxia with (1)(8)fluoromisonidazole (F-miso) before and during radiotherapy in patients with non-small-cell lung cancer (NSCLC): a pilot study. Radiother. Oncol. 2011; 98:109–16. [PubMed: 21056487]

Verhaeghe, J.; D'asseler, Y.; Staelens, S.; Lemahieu, I. Noise properties of simultaneous dual tracer PET imaging; IEEE Nuclear Sci. Symp. and Medical Imaging Conf.; Puerto Rico. 2005; Oct 23-29. 2005 p. 2611-4.

Wilson, JW.; Turkington, TG.; Colsher, JG.; Borges-Neto, S.; Reiman, RE.; Coleman, RE. Optimizing sequential dual tracer P.E.T. studies using a combined 2D/3D imaging protocol; IEEE Nuclear Sci. Symp. and Medical Imaging Conf.; Rome. 2004; Oct 16-22. 2004 p. 3357-60.2004

Xu B, et al. Can multimodality imaging using 18F-FDG18F-FLT PETcT benefit the diagnosis and management of patients with pulmonary lesions? Eur. J. Nucl. Med. Mol. Imaging. 2011; 38:285–92. [PubMed: 20936411]

Yamamoto Y, Nishiyama Y, Kimura N, Ishikawa S, Okuda M, Bandoh S, Kanaji N, Asakura M, Ohkawa M. Comparison of (18)F-FLT PET and (18)F-FDG PET for preoperative staging in non-small cell lung cancer. Eur. J. Nucl. Med. Mol. Imaging. 2008; 35:236–45. [PubMed: 17909790]

Yang W, Zhang Y, Fu Z, Yu J, Sun X, Mu D, Han A. Imaging of proliferation with 18F-FLT PET/CT versus 18F-FDG PET/CT in non-small-cell lung cancer. Eur. J. Nucl. Med. Mol. Imaging. 2010; 37:1291–9. [PubMed: 20309686]

Zander T, et al. Early prediction of nonprogression in advanced non-small-cell lung cancer treated with erlotinib by using [(18)F]fluorodeoxyglucose and [(18)F]fluorothymidine positron emission tomography. J. Clin. Oncol. 2011; 29:1701–8. [PubMed: 21422426]

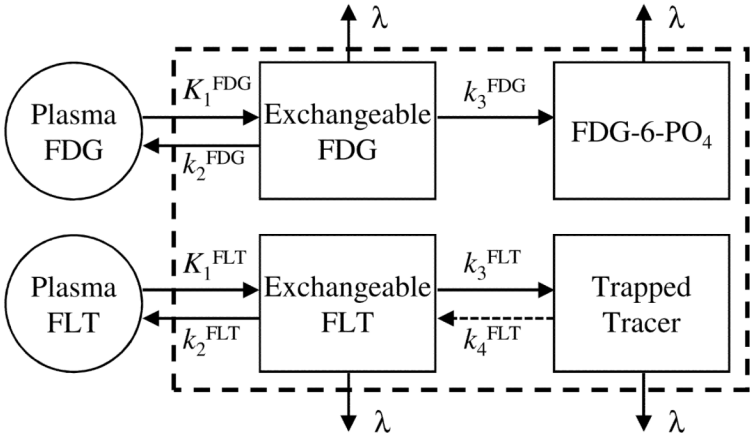

Figure 1.

Compartment models for FDG (top) and FLT (bottom), shown with the effects of radioactive decay (λ) included with the models. The dashed box represents parallel multi-tracer compartment modeling for temporally overlapping dual-tracer FDG+FLT time-activity curves. Here, the inputs for each tracer drive each model separately in the conventional sense, but the PET measurement comprises the sum of all tissue compartments including both tracers.

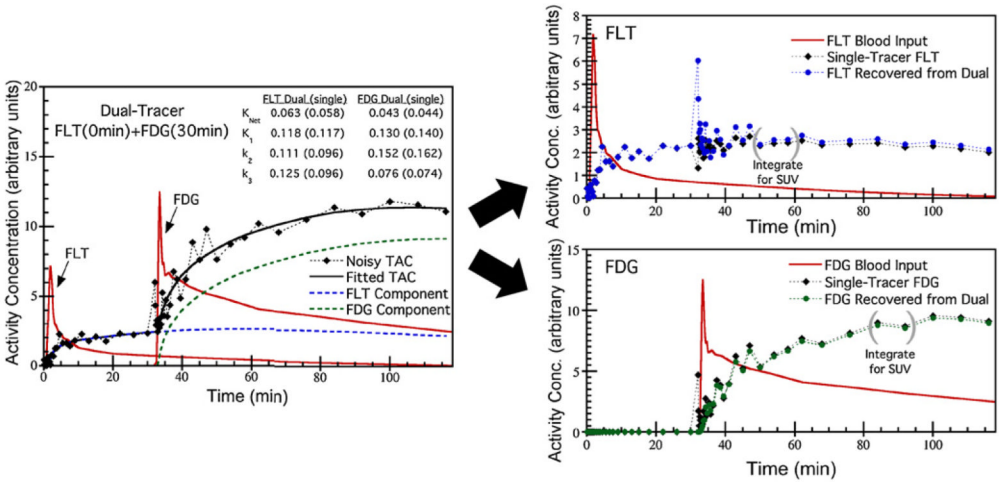

Figure 2.

Simulation study example showing a dual-tracer FLT(0 min)+FDG(30 min) time-activity curve and kinetic model fit (left), and recovered FLT and FDG components (right). The dual-tracer fit results are shown, along with the corresponding single-tracer fits in parenthesis. Using explicit signal separation, the noisy dual-tracer TAC is separated into estimated TACs for each individual tracer. Note the noise structure in the recovered TACs, especially in the FLT TAC around 30 min where short timeframes corresponding to the FDG injection result in high noise levels; these timeframes could be collapsed to long timeframes with lower noise in the recovered FLT TAC as desired. Static image values, e.g. SUVs, can be recovered for each tracer by integrating the recovered TACs as indicated.

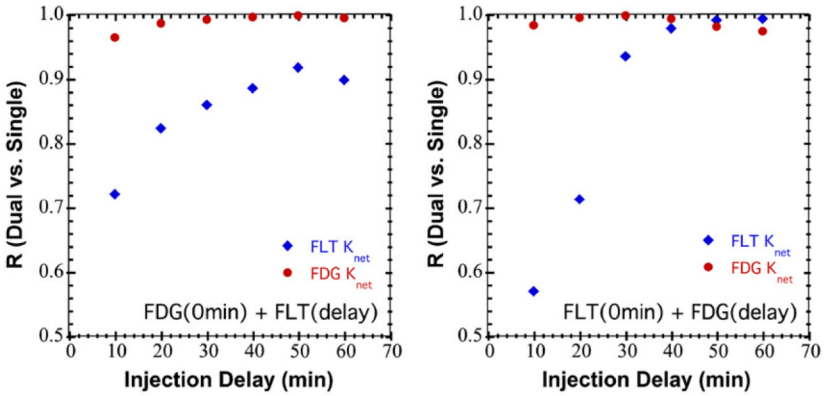

Figure 3.

Plots summarizing the effect of changing injection order and injection delay on the Pearson correlation coefficient (R) for recovering K_{net} from dual-tracer TACs as compared to single-tracer TACs. The data are shown for the simulation studies in which 200 pairs of noisy TACs with randomly selected rate parameters were analyzed for dual-tracer versus single-tracer performance. The plot on the left shows results for FDG administered first and FLT after various injection delays, and the plot on the right shows analogous results for FLT administered first. In both cases, recovery of K_{net} for FLT was highly dependent on the injection delay, improving with increasing delay, whereas recovery of FDG K_{net} was relatively insensitive to the delay used. Administering FLT first provided significantly better performance for injection delays of 30 min and longer.

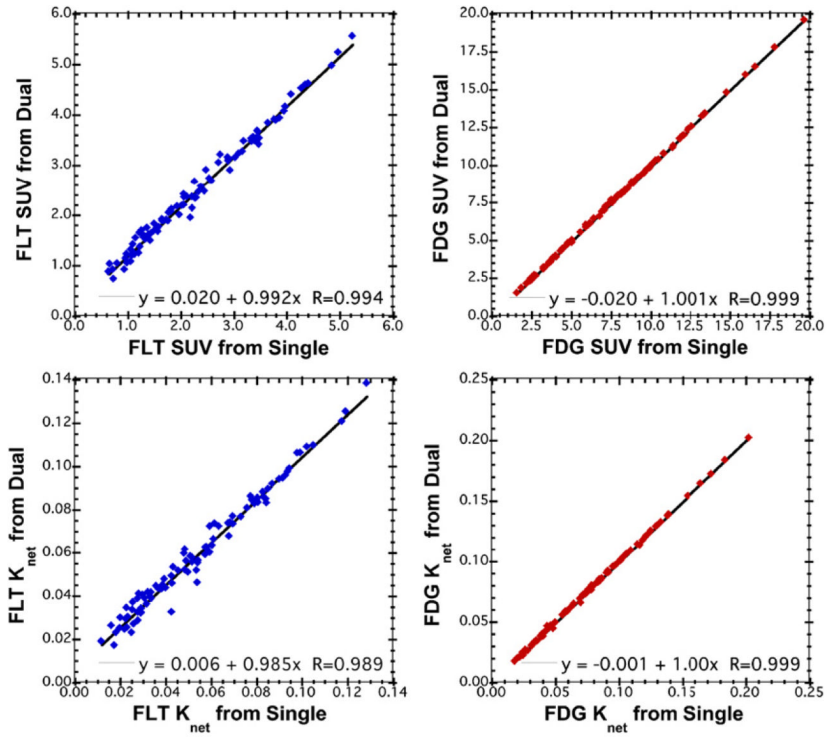

Figure 4.

Scatter plots comparing SUVs (top row) and net-uptake macroparameters (bottom row) recovered from the single-scan FLT(0 min) + FDG(30 min) simulated datasets. The component single-tracer datasets were used as the standards, offering paired signal and noise for the comparison. The recovered FDG parameters were nearly identical to the single-tracer results, and the FLT parameters were also recovered with excellent correlations, slopes and intercepts as shown in the plots.

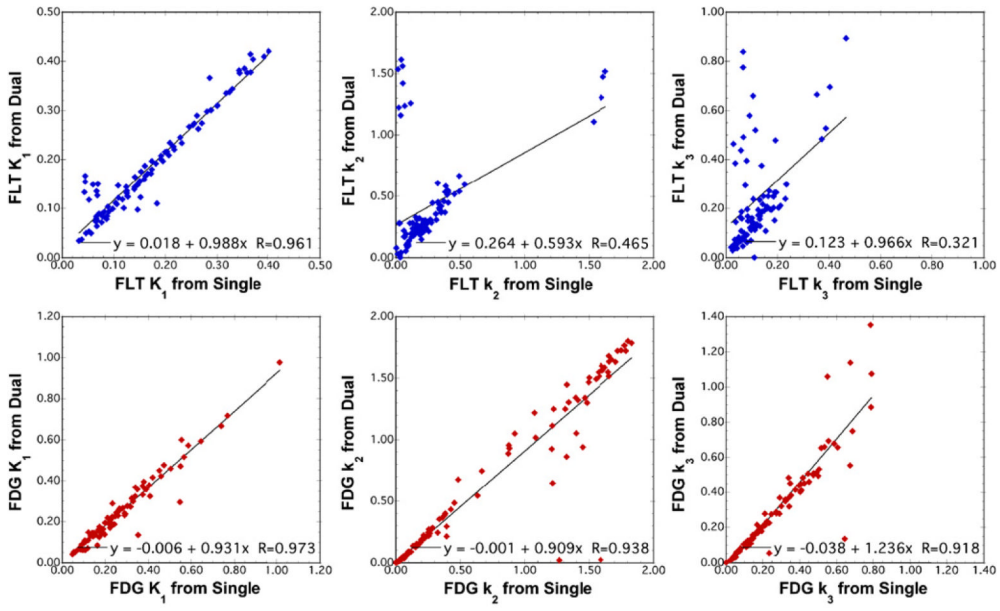

Figure 5.

Scatter plots for the simulation studies comparing recovery of kinetic microparameters for each tracer versus those calculated from the single-tracer datasets. The wash-in rate parameter was well recovered for both tracers, and k_2 and k_3 were also generally well-recovered for FDG but with some outliers. However, the recovered values of k_2 and k_3 for FLT had a large number of outliers, and recovery of these kinetic rate parameters from dual-tracer imaging was not considered robust.

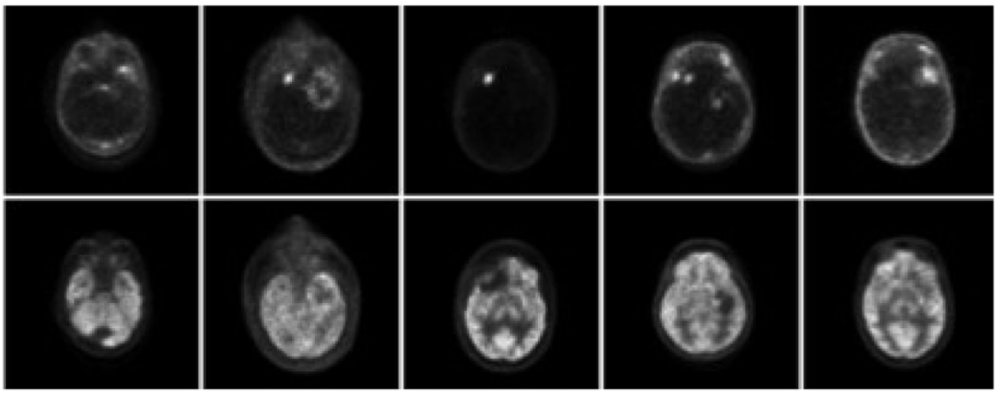

Figure 6.
Example PET images with FLT (top row) and FDG (bottom row) for each of the five brain tumor patients, where static images were created by combining timeframes from 50 to 60 min post-injection. Regions-of-interest were drawn on both tumor and normal brain regions, where multiple ROIs were used for large, heterogeneous tumors. The patient evaluation study tested performance for recovering both static and dynamic imaging measures for each of these regions.

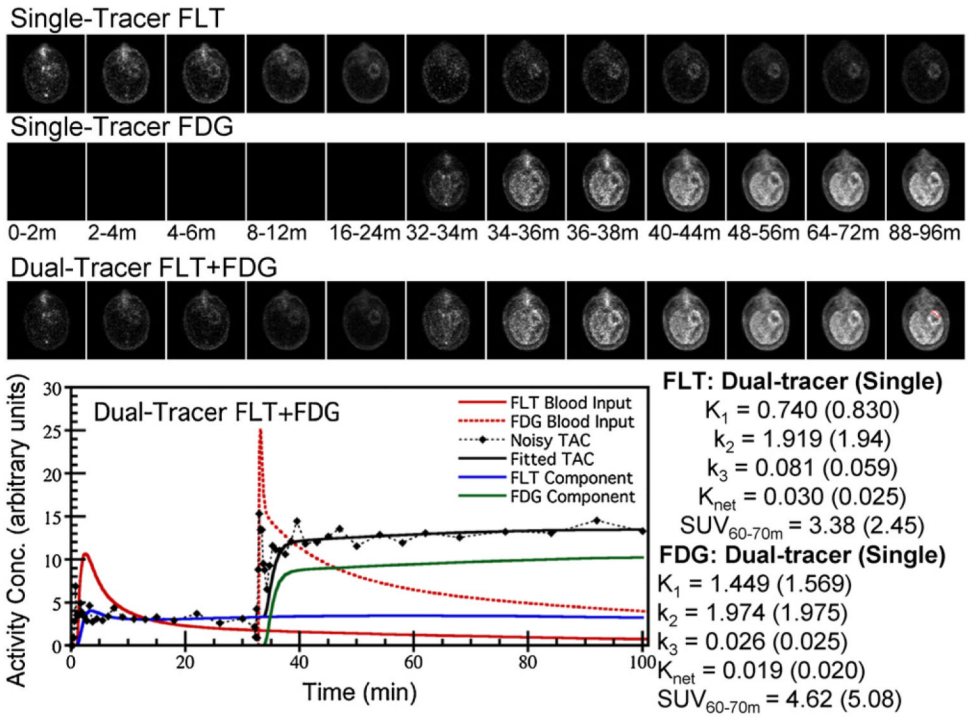

Figure 7.

Example dynamic PET images in one patient for single-tracer FLT, single-tracer FDG and dual-tracer FLT(0 min)+FDG(32 min), where all images are shown aligned in time with the dual-tracer temporal sequence. The plot shows the dual-tracer TAC for the ROI pictured in the final timeframe of the dual-tracer images (red), and fit results for both dual-tracer and separate single-tracer modeling (parenthesis) are shown at right.

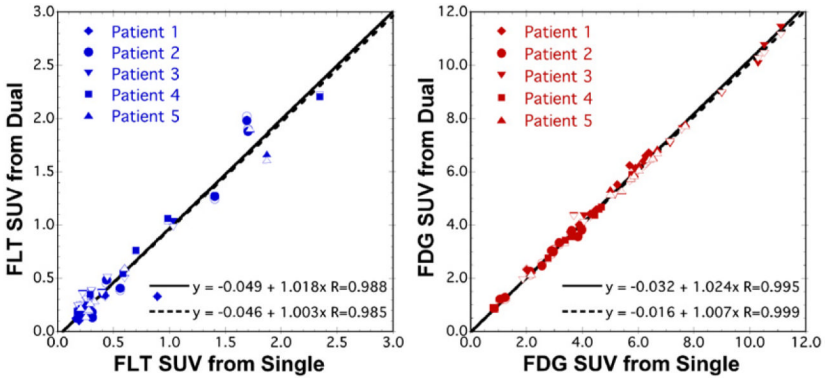

Figure 8.

Recovery of static image SUVs for dual-tracer FLT(0 min)+FDG(32 min) imaging in the brain tumor patients for ROIs drawn on both tumor and normal brain regions. The filled symbols and solid regression line are for SUVs computed by integrating the fitted TACs from 50 to 60 min post-injection, whereas the open symbols and dashed regression lines are for SUVs computed using the explicit signal-separation method of equation (6). Excellent recovery was obtained for both tracers, with correlations $R \geq 0.99$ and little bias noted in the linear regression analysis.

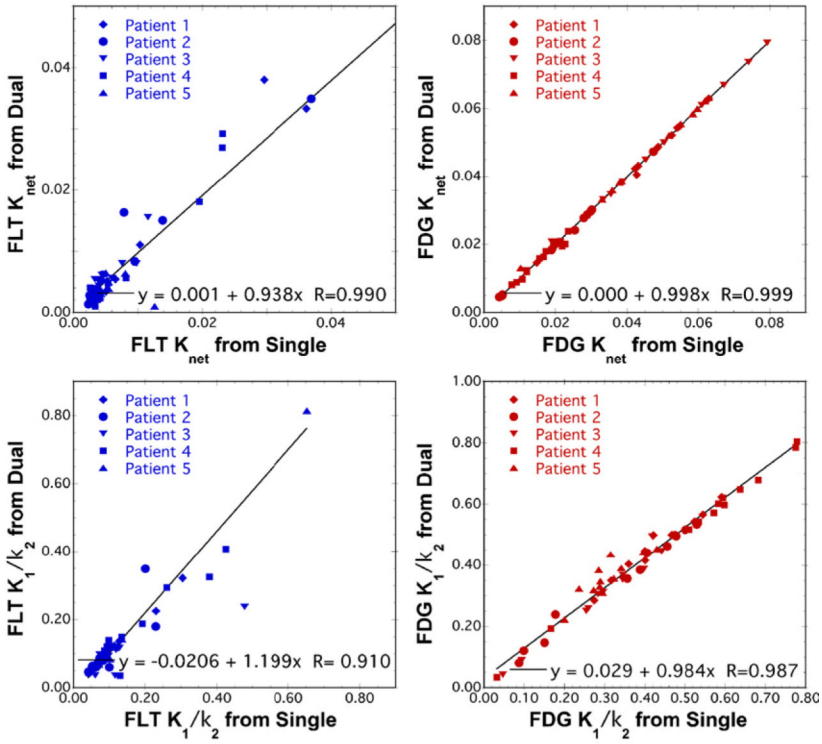

Figure 9.

Scatter plots comparing dual-versus single-tracer kinetic macroparameter estimates from the brain tumor patient images for ROIs drawn on both tumor and normal brain regions. The net uptake macroparameter was recovered with excellent correlations and little bias for both tracers. The K_1/k_2 macroparameter had correlation coefficients $R \geq 0.91$, although the recovered values of this parameter for FLT were biased with slope = 1.199. Results of the linear regression analysis for individual kinetic microparameters are provided in table 1.

Table 1

Recovery of kinetic microparameters for the patient studies.

	Range	Slope	Intercept	*R*
FLT				
K_1 (mL min^{-1} g^{-1})	[0.01, 3.7]	0.999	0.024	0.991
k_2 (min^{-1})	[0.01, 6.81]	0.925	0.292	0.978
k_3 (min^{-1})	[0.0, 0.85]	0.382	0.038	0.837
FDG				
K_1 (mL min^{-1} g^{-1})	[0.02, 5.02]	0.999	−0.052	0.995
k_2 (min^{-1})	[0.16, 6.84]	0.974	−0.122	0.968
k_3 (min^{-1})	[0.01, 0.95]	1.034	−0.009	0.994